Pergamon

PII : S0017–9310(96)00306–7

Metal-droplet deposition model including liquid deformation and substrate remelting

R. H. RANGEL and X. BIAN

Department of Mechanical and Aerospace Engineering and Department of Chemical and
Biochemical Engineering and Materials Science, University of California, Irvine, CA 92697,
U.S.A.

Abstract—A heat transfer model for metal-droplet deposition and solidification is developed. When a molten droplet arrives at the substrate, it undergoes deformation and solidification. The rates of deformation and solidification are, in general, of the same order of magnitude, so it is important to be able to predict the coupled behavior involving fluid deformation, heat transfer and solidification. Typical existing models have either neglected the deformation by assuming that it takes place fast or have used prescribed solutions of the solidification problem decoupled from the fluid dynamics. The present work describes a model which includes a solution of the mechanical energy equation containing kinetic and potential energy as well as viscous dissipation. In addition, the transient, convective-diffusive energy equation including viscous dissipation is solved in the deforming liquid phase by means of finite differences after appropriate coordinate transformations. The solid-phase transient energy equation is also solved in a transformed domain and the liquid and solid solutions are coupled to predict the actual growth of the solidification front. Because the solid energy equation is solved in the complete domain, which includes the substrate, it is possible to predict the behavior when remelting of the substrate occurs. Parametric studies are presented for a variety of relevant processing parameters. © 1997 Elsevier Science Ltd. All rights reserved.

1. INTRODUCTION

Thermal spray deposition is an efficient means of generating thin films for the purpose of increasing surface corrosion resistance or developing a thermal barrier. In addition, metal droplet deposition techniques have been applied in the manufacture of free-form, near net-shape structures in the process of microcasting [1].

Various experimental and theoretical studies have been conducted to investigate the spray deposition processes. An experimental study of the solidification of molten metal droplets impinging on a cold surface was reported in the work of Inada and Yang [2] who described the solidification behavior of molten lead droplets on a cold quartz or copper substrate. The interfacial thermal resistance for molten metal solidification on a substrate was investigated experimentally by Wang and Matthys [3] and Liu *et al.* [4]. El-Kaddah *et al.* [5] derived a one-dimensional analytical solution to the plasma spray process based on the Stefan model and obtained the two-dimensional profile of the spray solidification front numerically with that solution. Madejski [6] proposed a splat deformation and solidification model for the droplet deposition process in which the liquid phase of the splat assumes the shape of a cylinder. Instead of solving the thermal energy equation, Madejski used the solution of the Stefan solidification problem to predict the solid-front location. An improvement over Madejski's solution has been presented by Delplanque and Rangel [7] utilizing a more appropriate velocity profile

suggested by Markworth and Saunders [8] and an accurate derivation of the viscous energy dissipation. Numerical simulations utilizing the solution of the Stefan solidification problem to study the droplet deposition processes can be found in the work of Watanabe *et al.* [9], San Marchi *et al.* [10], Liu *et al.* [11], and Amon and Schmaltz [12]. A disadvantage of applying the Stefan solution is due to the fact that it does not take into account the motion and the finite thickness of the liquid phase on the solid–liquid interface evolution. Numerical studies of the solidification of a molten metal droplet impinging on a solid substrate can also be found in the work of Waldvogel *et al.* [13] and Kang *et al.* [14] in which the conductive thermal energy equations for the droplet and substrate were solved to determine the thermal behavior of the droplet and substrate. In addition, reported investigations of the droplet deposition process addressing the phenomena of substrate remelting have not taken into account the effect of liquid motion [12–15]. The effect of liquid motion on the solidification behavior during deposition processes has been investigated by Rangel and Bian [16, 17] through the study of the stagnation-flow solidification problem.

This work presents a droplet deformation and solidification model which includes a solution of the mechanical energy equation (containing kinetic and potential energy as well as viscous dissipation) based on the model of Madejski. In addition, the transient, convective–diffusive energy equation including viscous dissipation is solved in the deforming liquid

NOMENCLATURE

a_α ratio of the liquid to solid-phase thermal diffusivity, $a_\alpha = \alpha_l/\alpha_s$

a_k ratio of the liquid to solid-phase thermal conductivity, $a_k = k_l/k_s$

b liquid disk height

c specific heat

c_t transformation coefficient

d droplet diameter

Ec Eckert number, $Ec = w^2/c(T_i - T_m)$

E_k kinetic energy

E_p potential energy

E_Φ dissipated energy

Pr Prandtl number, $Pr = \nu/\alpha_l$

r radial coordinate (parallel to the substrate)

R splat radius

Re Reynolds number, $Re = \rho w d/\mu$

s solid-front height

s_{rm} maximum remelting depth

t time

u_r radial-velocity component (parallel to the substrate)

u_z normal-velocity component (perpendicular to the substrate)

v volume

V_s solidified volume fraction

V_{rm} remelted volume fraction

w droplet impinging velocity

z spatial coordinate perpendicular to the substrate.

Greek symbols

α thermal diffusivity

η_l transformed coordinate, $\eta_l = (2/\pi)\arctan[(\tilde{z} - \tilde{s})/\tilde{b}]$

η_s transformed coordinate, $\eta_s = (2/\pi)\arctan[c_t(\tilde{z} - \tilde{s})]$

ξ transformed coordinate, $\xi = \tilde{r}/\tilde{R}$

σ surface tension coefficient

ρ density

Φ dissipation function

ε ratio of initial splat radius to droplet diameter

θ nondimensional temperature, $\theta = (T - T_m)/(T_m - T_0)$

τ nondimensional time, $\tau = \tilde{t}$.

Subscripts

i   initial

l   liquid phase

o   substrate

m   melting

p   iteration index

s   solid phase.

Diacritical mark

$\sim$ nondimensional.

phase by means of finite differences after appropriate coordinate transformations. The solid-phase transient energy equation is also solved in a transformed domain, and the liquid and solid solutions are coupled to predict the actual growth of the solidification front. In addition to addressing the effect of liquid motion on the splat deformation and solidification process, the model can be applied to study the mechanism of substrate remelting. Parametric studies are presented for a variety of relevant processing parameters such as the initial droplet temperature, the initial substrate temperature, the initial droplet diameter as well as the droplet impinging velocity.

2. PHYSICAL AND MATHEMATICAL MODEL

A liquid metal droplet with initial temperature T_i, diameter d and velocity w impinges on a flat substrate whose initial temperature is T_0. Based on Madejski's original model [6], it is assumed that at $t = 0$, the incompressible liquid droplet assumes the shape of a cylindrical disk of radius R_0 and height b_0. The liquid splat then deforms by spreading radially with a phase-change process (solidification or remelting) occurring at the splat-substrate interface. The height of the

liquid phase, while being a function of time, is assumed uniform in space. A schematic plot of the model is shown in Fig. 1. Furthermore, properties are assumed constant but different in each phase, except for the density which is assumed constant throughout. The mechanical-energy equation governing the motion of the liquid disk is [7]

$$\frac{d}{dt}(E_k + E_p) = -\frac{dE_\Phi}{dt}, \qquad (1)$$

where E_k and E_p represent the kinetic energy and surface-tension potential energy, respectively,

$$E_k = 2\pi \int_0^R \int_0^b \frac{1}{2}\rho(u_r^2 + u_z^2)\,dz\,r\,dr \qquad (2)$$

$$E_p = \sigma(\pi R^2 + 2\pi R b), \qquad (3)$$

while the rate of viscous dissipation is given by:

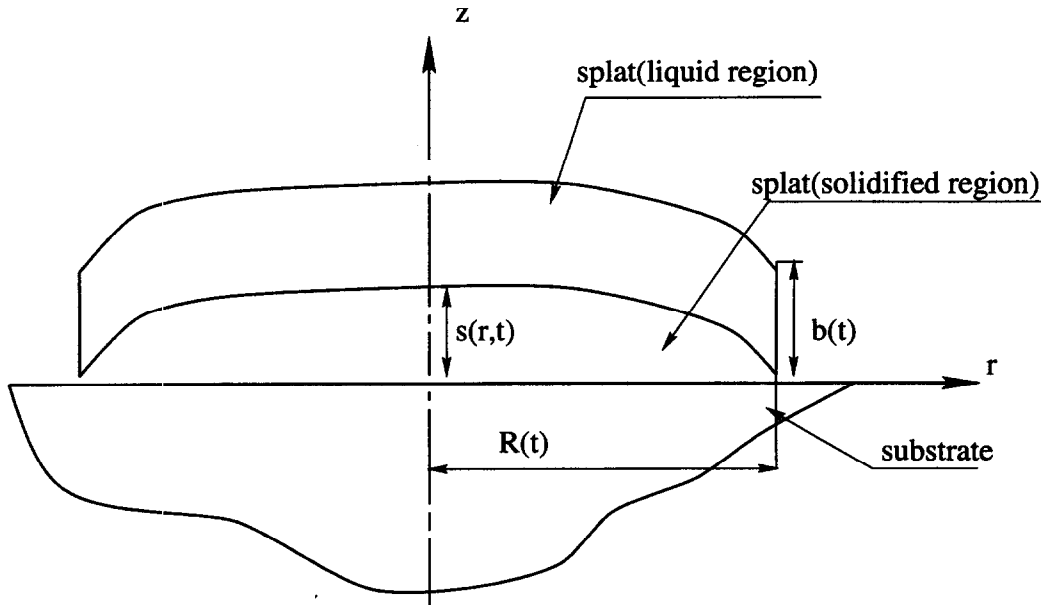$$\frac{dE_\Phi}{dt} = \int_v \mu\Phi\,dv, \qquad (4)$$

where

Fig. 1. Schematic of the problem and coordinate system.

$$\Phi = 2\left(\frac{\partial u_r}{\partial r}\right)^2 + 2\left(\frac{\partial u_z}{\partial z}\right)^2 + \left(\frac{\partial u_r}{\partial z} + \frac{\partial u_z}{\partial r}\right)^2 + 2\left(\frac{u_r}{r}\right)^2$$

$$(5)$$

is the viscous-dissipation function [18].

Within the liquid region, a velocity field which satisfies the continuity equation was proposed by Madejski [6]. Later, Markworth and Saunders [8] proposed a better velocity profile which, in addition to satisfying the equation of continuity, also satisfies the shear-free condition on the free surface of the liquid

$$u_r = Dr(2zb - z^2), \quad u_z = 2D\left(\frac{z^3}{3} - bz^2\right),$$

$$(6)$$

where D is a function of time to be determined by assuming that the rate of increase of the splat radius is equal to the average radial liquid velocity at the edge of the splat

$$\frac{dR}{dt} = \frac{1}{b}\int_0^b u_r(R, z)\,dz$$

$$= \frac{1}{b}\int_0^b DR(2zb - z^2)\,dz = \frac{2}{3}DRb^2 \qquad (7)$$

from which the function D is related to the spreading rate. Employing the velocity profile (6), the kinetic energy E_k can be expressed as:

$$E_k = \left(\tfrac{2}{15}b^5R^4 + \tfrac{22}{105}b^7R^2\right)\pi D^2\rho \qquad (8)$$

while rate of viscous-dissipation becomes

$$\frac{dE_\Phi}{dt} = \frac{\pi\mu R^2}{b}\left(\frac{dR}{dt}\right)^2\left(\frac{3}{2} + \frac{72}{5}\frac{b^2}{R^2}\right). \qquad (9)$$

Incorporating eqns (3), (8) and (9) into the mechanical energy eqn (1) and employing dimensionless variables such that time, length and velocity are non-dimensionalized with d/w, d and w, respectively, yields:

$$\frac{d}{d\tilde{t}}\left[\frac{3}{10}\left(\frac{d\tilde{R}}{d\tilde{t}}\right)^2 \tilde{b}\left(\tilde{R}^2 + \frac{11}{7}\tilde{b}^2\right) + \frac{\tilde{R}}{We}(\tilde{R} + 2\phi)\right]$$

$$+ \frac{\tilde{R}^2}{\tilde{b}Re}\left(\frac{d\tilde{R}}{d\tilde{t}}\right)^2\left(\frac{3}{2} + \frac{72}{5}\frac{\tilde{b}^2}{\tilde{R}^2}\right) = 0. \qquad (10)$$

The height of the liquid disk is determined from the mass conservation relation,

$$\frac{\pi}{6}d^3\rho = \pi R^2 b\rho + \int_0^R 2\pi r s\rho\,dr \qquad (11)$$

or, in dimensionless form

$$\tilde{b} = \frac{1}{6\tilde{R}^2} - \frac{1}{\tilde{R}}\int_0^{\tilde{R}} 2\tilde{r}\tilde{s}\,d\tilde{r}. \qquad (12)$$

At $t = 0$, the mass of the splat as well as its kinetic and potential energies are assumed equal to the corresponding values for the droplet:

$$\frac{\pi}{6}d^3\rho = \pi R_0^2 b_0\rho \qquad (13)$$

$$E_k(0) = \frac{1}{2}\rho\frac{\pi d^3}{6}w^2 = \left[\frac{2}{15}b_0^5R_0^4 + \frac{22}{105}b_0^7R_0^2\right]\pi D_0^2\rho$$

$$(14)$$

$$E_p(0) = \pi d^2\sigma = (\pi R_0^2 + 2\pi R_0 b_0)\sigma. \qquad (15)$$

If the initial radius of the disk is expressed as a fraction of the droplet diameter, $R_0 = \varepsilon d$, the initial conditions for this set of integral-differential equations are:

$$\tilde{R}_0 = \varepsilon, \quad \bar{b}_0 = \frac{1}{6\varepsilon^2}, \quad \frac{d\tilde{R}}{d\tilde{t}}\bigg|_{\tilde{t}=0} = \sqrt{\cfrac{1}{\cfrac{3}{5} + \cfrac{11}{420\varepsilon^6}}}.$$

(16)

Equations (13) and (15) yield $\varepsilon = 0.74$ whereas Madejski assumed $\varepsilon = 0.5$, apparently not recognizing that the exact solution $\varepsilon = 0.74$ exists [7].

The non-dimensional form of the liquid-phase thermal-energy equation including all previously noted assumptions and neglecting conduction in the radial direction, is

$$\frac{\partial \theta_1}{\partial \tilde{t}} + \tilde{u}_z \frac{\partial \theta_1}{\partial \tilde{z}} + \tilde{u}_r \frac{\partial \theta_1}{\partial \tilde{r}} = \frac{1}{RePr} \frac{\partial^2 \theta_1}{\partial \tilde{z}^2} + \frac{Ec}{Re} \theta_1 \tilde{\Phi} \qquad (17)$$

in the domain $0 \leqslant \tilde{r} \leqslant \tilde{R}$, $\tilde{s} < \tilde{z} \leqslant \tilde{s} + \bar{b}$, $\tilde{t} > 0$, and with boundary conditions $\theta_1 = 0$ at $\tilde{z} = \tilde{s}$, $\partial \theta_1/\partial \tilde{r} = 0$ at $\tilde{r} = 0$ and $\tilde{r} = \tilde{R}$, and $\partial \theta_1/\partial \tilde{z} = 0$ at $\tilde{z} = \tilde{s} + \bar{b}$.

The neglect of radial conduction is justified on the basis that the initial temperature field consists of isotherms which are parallel to the radial direction and the fact that the deformation results mostly in the formation of a nearly horizontal splat. Convection and radiation from the liquid surface are also neglected. Under similar assumptions, the dimensionless solid-phase thermal-energy equation is

$$\frac{\partial \theta_s}{\partial \tilde{t}} = \frac{1}{a_\alpha RePr} \frac{\partial^2 \theta_s}{\partial \tilde{z}^2} \qquad (18)$$

with the corresponding solution domain: $-\infty < \tilde{z} < \tilde{s}$, $\tilde{r} > 0$, and with boundary conditions: $\theta_s \to -1$ as $z \to -\infty$, $\theta_s = 0$ at $\tilde{z} = \tilde{s}$ and $\partial \theta_s/\partial \tilde{r} = 0$ at $\tilde{r} = 0$ and $\tilde{r} = \tilde{R}$.

The energy balance equation at the interface $\tilde{z} = \tilde{s}(\tilde{t}, \tilde{r})$ yields an expression for the variation of the dimensionless interface location with time

$$\frac{\partial \tilde{s}}{\partial \tilde{t}} = \frac{St}{RePr}\left[1 + \left(\frac{\partial \tilde{s}}{\partial \tilde{r}}\right)^2\right]\left[\frac{\partial \theta_s}{\partial \tilde{z}} - a_k \frac{\partial \theta_1}{\partial \tilde{z}}\right]. \qquad (19)$$

The above system of equations can be solved numerically to obtain the shape of the solid and liquid domains, the motion of the solid–liquid interface, and the temperature distributions in the solid and liquid phases.

3. NUMERICAL METHOD

The solution domains for this problem involve moving boundaries and the location of such boundaries must be determined as part of the solution. It is advantageous to transform the domains so that the problem

is converted to a fixed-boundary problem. By introducing the independent variables, τ, ξ and η_1 defined in the nomenclature, the liquid-phase domain becomes $0 \leqslant \xi \leqslant 1$, $0 \leqslant \eta_1 \leqslant 0.5$. Furthermore, by introducing the independent variables τ, ξ and η_s, the semi-infinite moving-boundary solid domain is mapped onto the finite region $0 \leqslant \xi \leqslant 1$, $-1 \leqslant \eta_s \leqslant 0$. The moving interface location is transformed to a fixed location $\eta_1 = \eta_s = 0$. The metrics of the transformations as well as the transformed equations are given in the Appendix.

Equations (A.9) and (A.10) are solved by the ADI method [19] to obtain the time evolution of the liquid- and solid-phase temperature fields with the liquid-phase velocity distribution provided by eqn (6). The time evolution of the solid-front location is obtained from eqn (A.11) by the modified Euler method. The time rate of change of the splat radius as well as the time rate of change of the liquid disk thickness are obtained by coupling the above-mentioned equations with eqns (10) and (12). The radial coordinate transformation ($\tilde{r} \to \xi$) introduces an advective term in the energy balance equation [first term on the RHS of eqn (A.11)]. For numerical stability this term is written using an upwind scheme. Other derivatives appearing in the energy equations are expressed with central difference formulas. The numerical solution of eqn (10) is described by Delplanque and Rangel [7] while eqn (12) is evaluated using the trapezoidal rule.

In all the calculations, 21 grid points are used in the ξ (radial) direction, while 31 grid points are used in the η_1 direction (liquid) and 21 grid points are used in the η_s direction (solid). The coefficient c_1, which clusters grid points near the solid–liquid interface is set to 20. The time step $\Delta\tau$ is 0.001 for the computation with the large (1 mm) droplets and 0.0001 for the computation with the small (0.1 mm) droplets. Tests with larger numbers of grid points yield essentially the same results.

4. RESULTS AND DISCUSSION

4.1. Base–case calculation

As a base–case calculation, the model is applied to investigate the deformation and solidification behavior of a liquid aluminum droplet impinging on a substrate of aluminum with an initially lower temperature. The base–case calculation corresponds to case 1 in Table 1, where the relevant parameters are listed.

The time evolution of the splat is displayed in Fig. 2 which illustrates the solidification behavior including the disk size, the liquid thickness, the solid-front location along the radial direction, as well as the relative ratio of the solid and liquid volume. Note that the scales are different on the left and right frames of this figure and that for all frames, the vertical scale exaggerates the actual thickness. During the final

Table 1. Parametric data

Case	d [mm]	w [ms^{-1}]	T_0 [K]	T_i [K]	θ_i	a_α	a_k	St	Re	We	Ec	Pr
1	1.0	10.0	300	1033	0.16	0.43	0.40	1.67	21 215	265.88	0.92×10^{-3}	0.13×10^{-1}
2	1.0	1.0	300	1033	0.16	0.43	0.40	1.67	2121	2.66	0.92×10^{-5}	0.13×10^{-1}
3	0.1	10.0	300	1033	0.16	0.43	0.40	1.67	2121	26.59	0.92×10^{-3}	0.13×10^{-1}
4	0.1	1.0	300	1033	0.16	0.43	0.40	1.67	212	0.26	0.92×10^{-5}	0.13×10^{-1}
5	1.0	10.0	883	1033	2.0	0.52	0.43	0.15	21 215	265.88	0.92×10^{-3}	0.13×10^{-1}
6	1.0	1.0	883	1033	2.0	0.52	0.43	0.15	2121	2.66	0.92×10^{-5}	0.13×10^{-1}
7	1.0	10.0	300	1950	1.61	0.49	0.46	1.67	40 105	322.10	0.91×10^{-4}	0.61×10^{-2}
8	1.0	10.0	300	2000	1.68	0.50	0.46	1.67	41 045	325.88	0.86×10^{-4}	0.61×10^{-2}
9	1.0	10.0	883	1050	2.34	0.52	0.43	0.15	21 583	266.74	0.79×10^{-3}	0.13×10^{-1}
10	1.0	10.0	883	1150	4.34	0.53	0.44	0.15	23 745	271.91	0.42×10^{-3}	0.12×10^{-1}
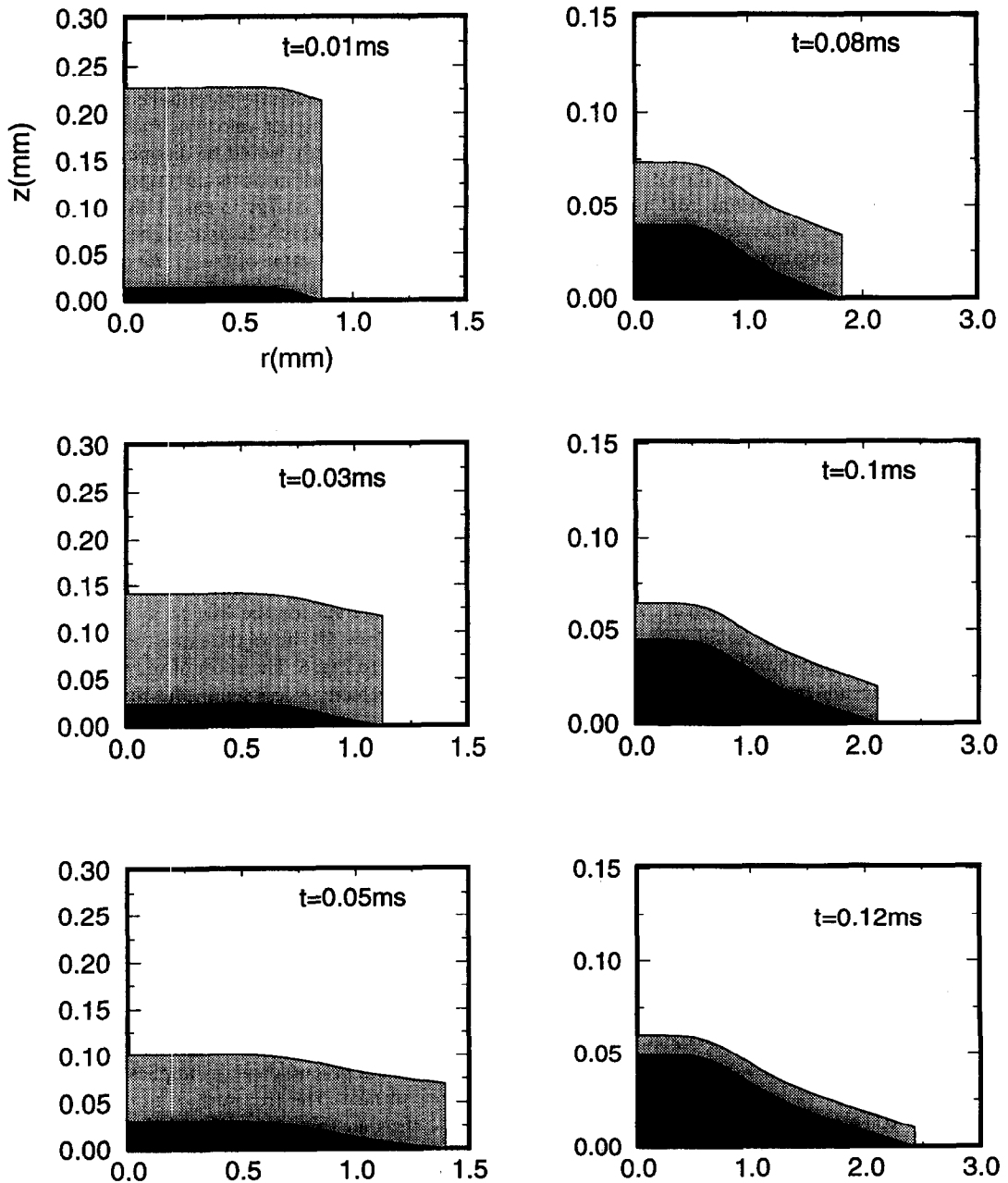
Fig. 2. Time evolution of the splat shape for case 1 (dark = solid, gray = liquid) ($d = 1$ mm, $w = 10$ m s^{-1}).

stages of solidification, the liquid portion becomes very thin in the vertical direction and the expansion of the disk radius diminishes correspondingly. The temperature distribution at selected times is shown in Fig. 3. The effect of heat penetration into the substrate is evident by the temperature gradient in the solid phase. The numerical domain actually extends to $-\infty$ into the substrate. At this low superheat (100 K above the melting point, melting temperature of 933 K), the liquid quickly achieves a nearly uniform temperature while the upper part of the substrate is heated significantly to several hundred degrees over the initial substrate temperature of 300 K. It should be noticed that the isothermal lines in both the liquid and solid phase are approximately horizontal (the vertical scale is exaggerated), which validates the neglect of radial conduction. The velocity field at selected times is provided in Fig. 4. It can be observed that as time increases and the thickness of the liquid phase decreases, the velocity gradient $\partial u_r/\partial z$ increases significantly, thus increasing the rate of dissipation of mechanical energy. As will be shown later, viscous dissipation plays an important role in consuming mechanical energy. However, at this impinging velocity, viscous dissipation plays a negligible role in the thermal field.

4.2. Effect of impinging velocity and droplet size

The time evolution of a splat with a lower impinging velocity (case 2) is shown in Fig. 5. The effect of the droplet impinging velocity on the deformation and solidification behavior is studied by comparing the time evolution of the splat radius (a), the splat expansion rate (b), the liquid thickness (c) and the solid-fraction (d) for cases 1 and 2 as shown in Fig. 6. The predictions of Madejski's model for these two cases are also included in Fig. 6 for comparison. As expected, the higher impinging velocity yields a larger solid splat. Moreover, the solidification process is completed after a longer time for the low velocity case. Madejski's model underpredicts the solidification time and the thickness of the liquid. It also overpredicts the solid fraction and generally overpredicts the expansion rate, except at the lower impinging velocity (1 m s^{-1}). The reason for this can be understood with the aid of Fig. 7, which shows the time evolution of the solid front along the axis of the splat. Madejski's model imposes a solidification rate given by the Neumann solution of the stagnant Stefan solidification problem. Such a solution neglects the effect of the liquid motion towards the substrate and this motion, which is similar to a stagnation flow, tends to reduce the solidification rate [16, 17]. The Schwarz solution as given in ref. [20] is better than the Neumann solution because it accounts for the heat transfer into the substrate. Nevertheless, it still overpredicts the solidification rate. The Neumann and Schwarz solutions also assume a semi-infinite liquid which by itself would underpredict the solidification rate. However, the velocity effect dominates the results. It is interesting to

note, however, that the solidification rates for cases 1 and 2 are almost identical along the splat axis. On one hand, a higher impinging velocity has the effect of reducing the solidification rate. On the other hand, a higher impinging velocity results in a thinner liquid which tends to solidify faster. The two effects combine to yield an almost independent solidification rate although the velocity effect dominates over the finite-liquid effect when compared with the Neumann and Schwarz solutions.

The time variation of the kinetic and potential energies as well as the time accumulation of the dissipated energy for cases 1 and 2 are shown in Fig. 8(a, b), respectively. As expected, kinetic energy decreases as potential energy increases with the increasing free-surface area. Viscous dissipation is an important factor in case 1 (higher velocity) but it is negligible in case 2 (low velocity). In this second case, all kinetic energy is transformed into potential energy of the free surface. At even higher velocities (not shown), most of the kinetic energy would be dissipated by friction. While viscous dissipation is an important factor in consuming kinetic energy in case 1 (higher velocity), the thermal effect of this dissipated energy is negligible in view of the low value of the Ec/Re ratio (see Table 1). Much higher impingement velocities and much smaller drop sizes would be required for heating due to viscous dissipation to become important.

The effect of droplet size is illustrated in Figs. 9–11 which present results for droplets with an initial diameter of 100 μm (cases 3 and 4). The results shown in Figs. 9–11 should be compared with those of Figs. 6–8, respectively. The results are qualitatively similar. Figure 9 shows that a factor of 10 reduction in the droplet diameter yields a factor of 20 reduction in the solidification time for the higher (10 m s^{-1}) impinging velocity and a factor of about 70 reduction in the solidification time for the low (1 m s^{-1}) impinging velocity. Figure 10 shows the same trends referred to in reference to Fig. 6. The effect of varying the droplet impinging velocity is less significant for smaller droplets.

Figure 11 shows the time variation of the kinetic, potential and dissipated energies for cases 3 and 4. Similarly to cases 1 and 2, the only difference between cases 3 and 4 is the impinging velocity. Thus the initial surface-tension potential energy is the same for cases 3 and 4 while the initial kinetic energy for case 3 is 100 times larger than for case 4. Again, viscous dissipation is negligible for the lower velocity (case 4), but this case shows an interesting trend almost imperceptible in case 2. During the initial stages of solidification, the kinetic energy of the liquid actually increases briefly while the potential energy decreases. A reduction in potential energy implies a reduction of the free surface. The free surface initially decreases despite the fact that the liquid is spreading because solidification reduces the amount of free surface and this effect initially dominates, particularly for smaller droplets and lower velocities.
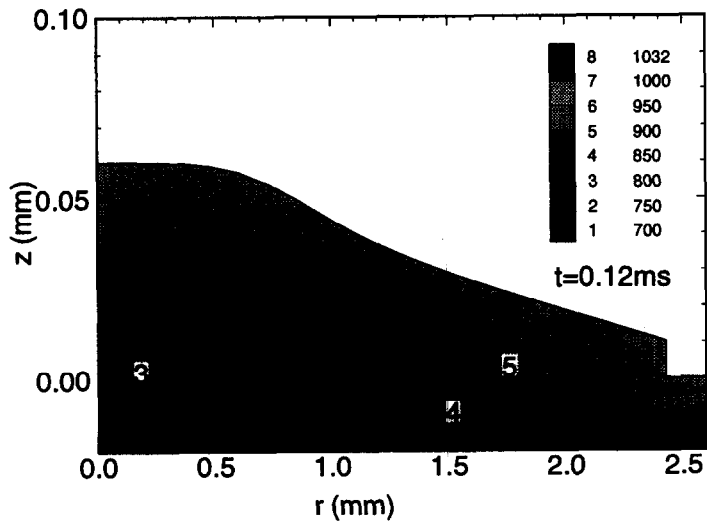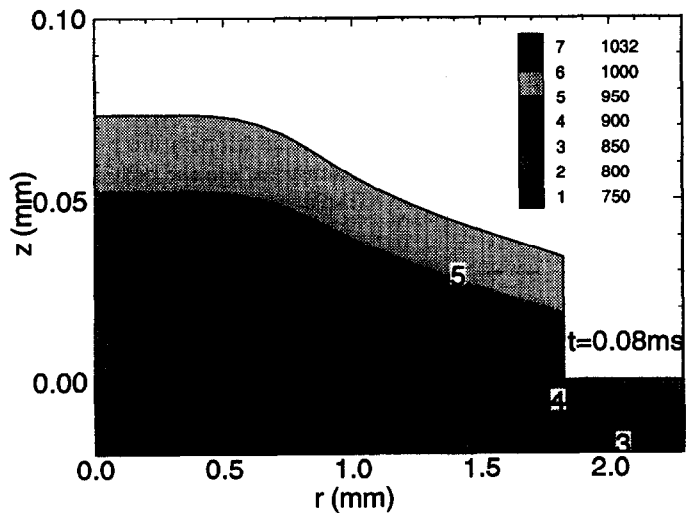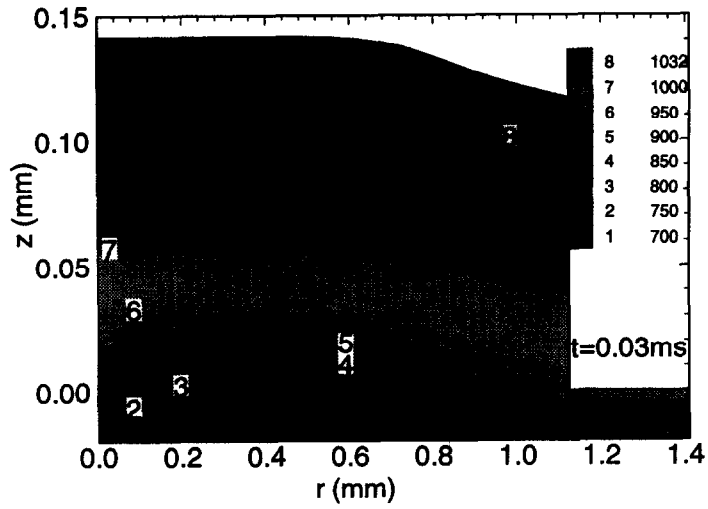
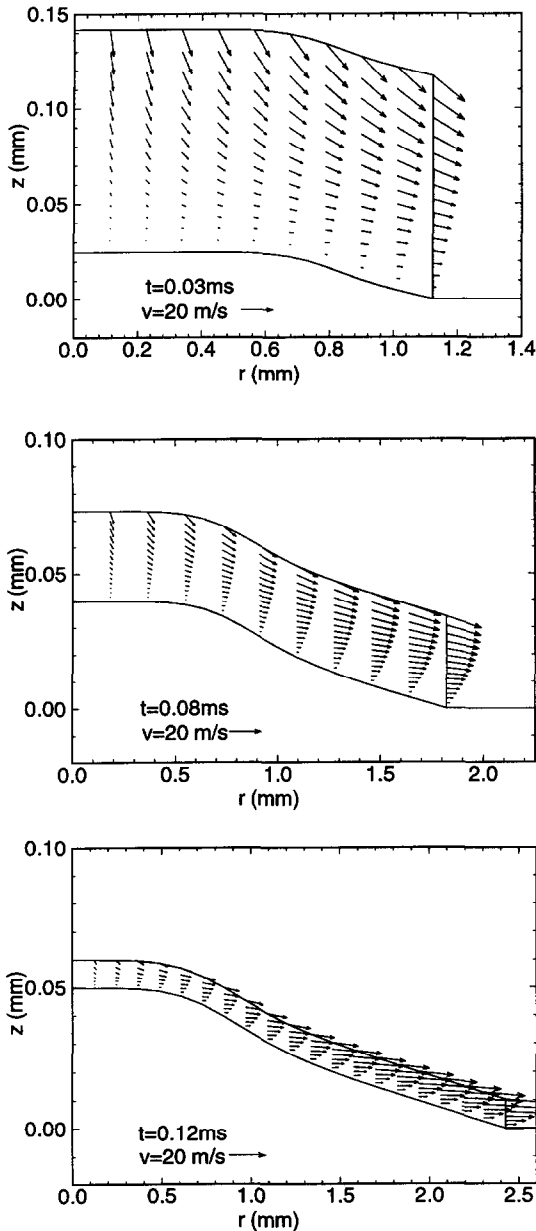Fig. 3. Temperature field in the liquid and upper substrate at selected times (case 1).

Fig. 4. Liquid velocity field at selected times (case 1).

4.3. Deposition with substrate remelting

Remelting of the substrate may play an important role in enhancing the bonding characteristics of the deposit. The onset of remelting upon droplet landing may actually be predicted using the Schwarz solution [20]. This is due to the fact that the onset of remelting is a local phenomenon at the initial liquid/substrate interface and it is affected by local conditions (temperature gradients). Over such a small length scale, the liquid and the substrate behave as semi-infinite media for very small times. The motion of the interface beyond the onset of remelting or solidification requires the solution of the thermal energy equations for the actual geometry [eqns (17)–(19)]. The criterion for remelting to occur when the liquid initial tem-

perature is T_i and the substrate initial temperature is T_0 is [20]:

$$\frac{T_i - T_m}{T_m - T_0} - \frac{\sqrt{a_\alpha}}{a_k} > 0. \tag{20}$$

For an aluminum liquid droplet with an initial temperature of 1033 K (100 K over its melting temperature), the initial substrate temperature must be above 880 K for remelting to occur upon droplet impingement.

To illustrate the various features of deposition with remelting, we consider cases 5–10 listed in Table 1. These cases show the effect of velocity and initial liquid and substrate temperature on the remelting behavior. The time evolution of the splat shape is provided in Fig. 12 for case 5. It can be observed that substrate remelting occurs during the early stages of the process. Because remelting occurs near the central portion of the splat (under the area covered by the initial disk) and not under the subsequent spreading, a depression of the solid front develops near the center. The temperature distributions at selected times for case 5 are provided in Fig. 13. It can be seen that the temperature profile is nearly parallel to the substrate and the region of the substrate close to the splat is significantly heated. Because the substrate temperature is close to the metal melting point, the middle and later stages of solidification occur at nearly isothermal conditions in this case.

The effect of impinging velocity on the remelting is shown in Fig. 14 (cases 5 and 6). At the lower velocity, a condition is reached in which the spreading rate (Fig. 14(b)) equals zero. At this time, the liquid thickness (Fig. 14(c)) reaches a local minimum. This corresponds to a condition of minimum surface area and implies that the liquid would recoil (negative expansion rate) beyond this time. Remelting may still proceed under the contracting splat but the present model cannot account for this behavior. Figure 14(d) shows the time evolution of the solidified and remelted volume fractions for these cases. The solidified volume fraction V_s is the ratio of the solidified volume above the initial surface of the substrate to the initial droplet volume. Likewise, the remelted volume fraction V_{rm} is the ratio of the remelted volume under the initial surface of the substrate to the initial droplet volume. For case 5, the maximum remelted fraction is slightly larger than 2%. The overlapping of the V_s and V_{rm} curves for case 5 indicates that the solid front is still under the initial substrate surface near the center of the splat while it is above the initial substrate surface near the outer edge of the splat. Comparing Figs. 6 and 14 (cases 1 and 5), it can be seen that remelting of the substrate by an initially hotter liquid droplet considerably increases the total solidification time, in this case by a factor of almost ten.

Figure 15 shows the effect of the initial liquid and substrate temperatures on the behavior of the solid front along the axis of the splat (cases 7–10 in Table 1).
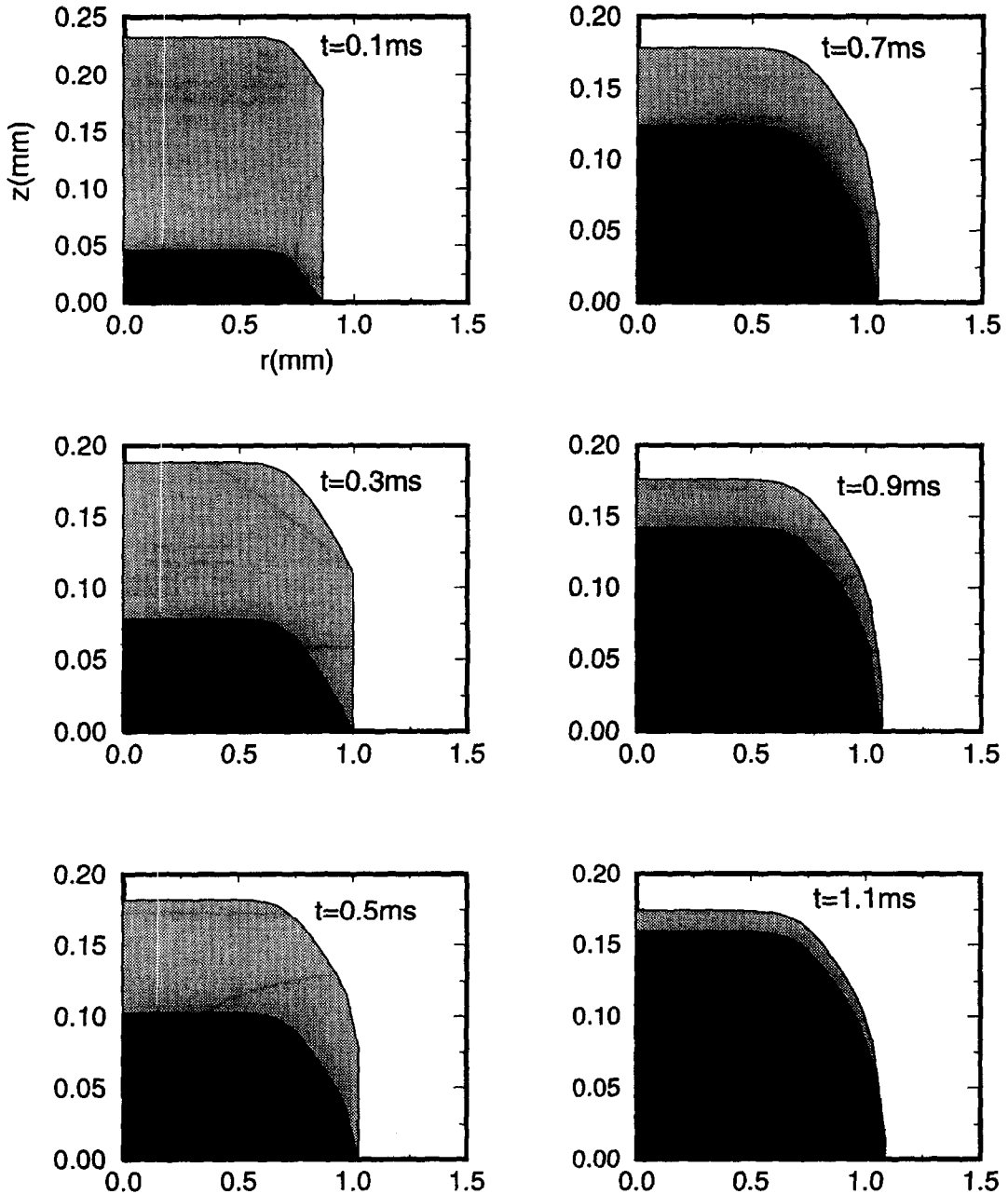
Fig. 5. Time evolution of the splat shape for case 2 (dark = solid, gray = liquid) ($d = 1$ mm, $w = 1$ m s^{-1}).

This figure shows that the time to reach the maximum remelting depth is fairly insensitive to the initial liquid temperature over a liquid temperature range of about 100–200 K. Sensitivity of this time to the initial substrate temperature is also small. The maximum remelting depth is more sensitive to the initial liquid temperature and in fact increases by a factor of 3 when the initial liquid temperature is increased by 100 K for the case of a substrate at 883 K. The maximum remelting depth for both low (300 K) and high (883 K) substrate temperature is a linear function of initial liquid temperature as illustrated in Fig. 16. The magnitude of the shape of this linear relation increases

with increasing substrate temperature or increasing droplet size.

5. CONCLUSIONS

A metal-droplet deformation and solidification model which includes the solution of the thermal-energy equations in both the liquid and solid phases has been developed to study the process of liquid metal droplet impinging on a flat substrate. Sample computations have been performed for liquid aluminum droplets with different initial sizes and velocities
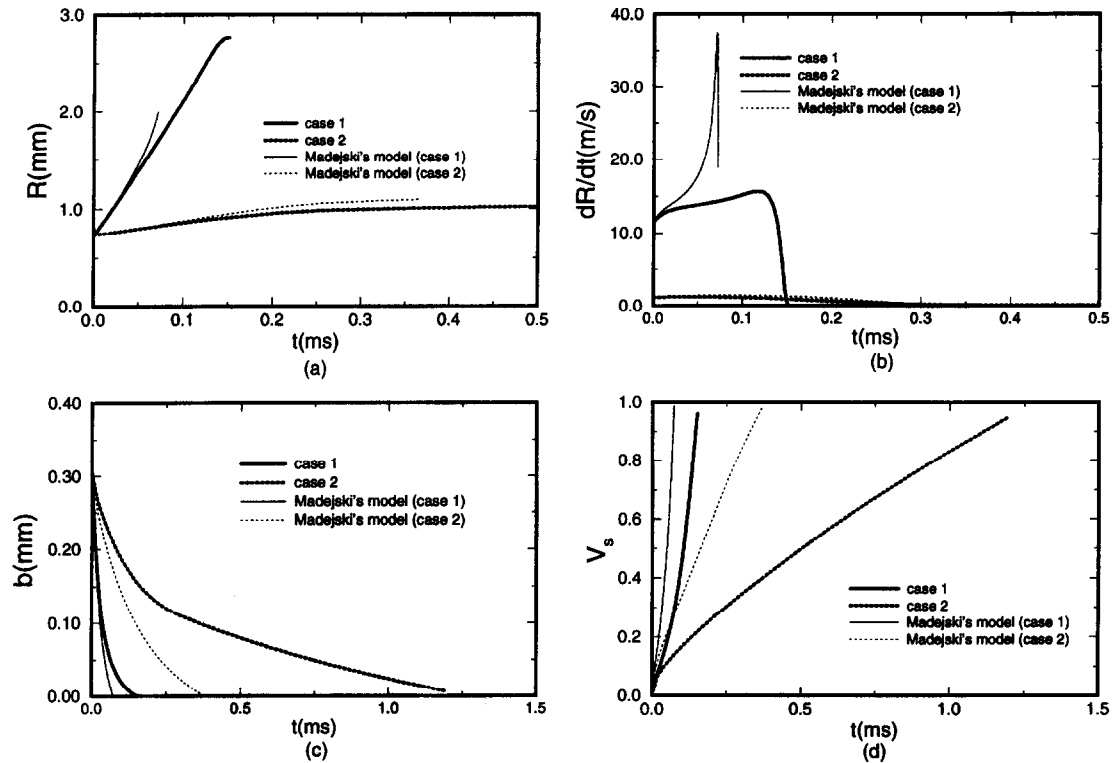
Fig. 6. Time evolution of: (a) splat radius; (b) radius expansion rate; (c) liquid thickness; and (d) solid
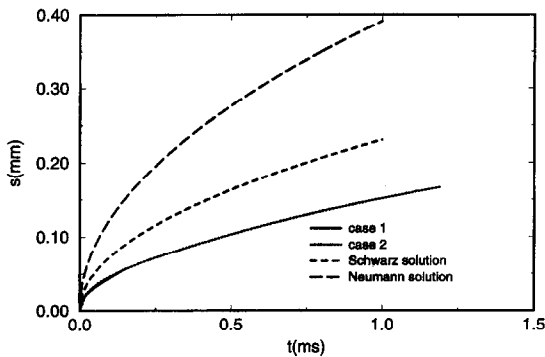fraction for cases 1 and 2.

Fig. 7. Time evolution of the solid-front location along the
splat axis for cases 1 ($w = 10 \text{ m s}^{-1}$) and 2 ($w = 1 \text{ m s}^{-1}$).

impinging on a colder substrate of the same material.
Furthermore, the phenomenon of substrate remelting
is investigated. The time evolution of the process vari-
ables such as disk radius expansion, the rate of expan-
sion, the liquid phase thickness, as well as the solid-
fraction location are obtained. The time evolution
of the splat mechanical energy is also investigated.
Increasing the impinging velocity will accelerate the
deformation and solidification process and increase
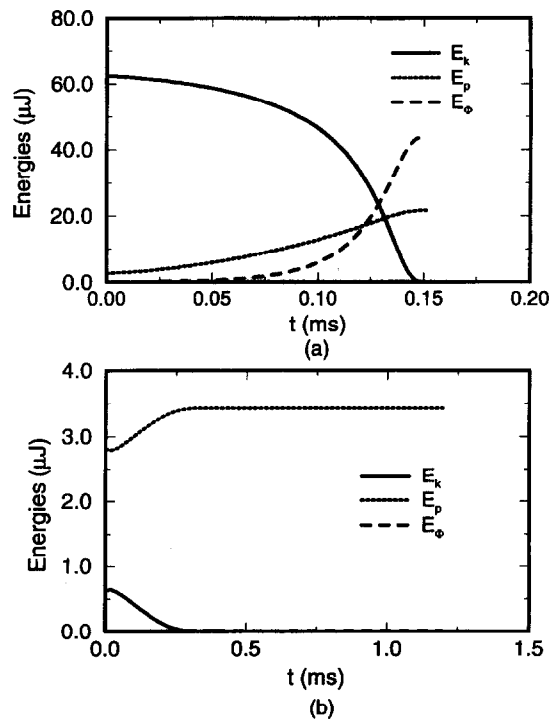the final disk radius while the final maximum solid-

Fig. 8. Time evolution of the liquid-phase mechanical
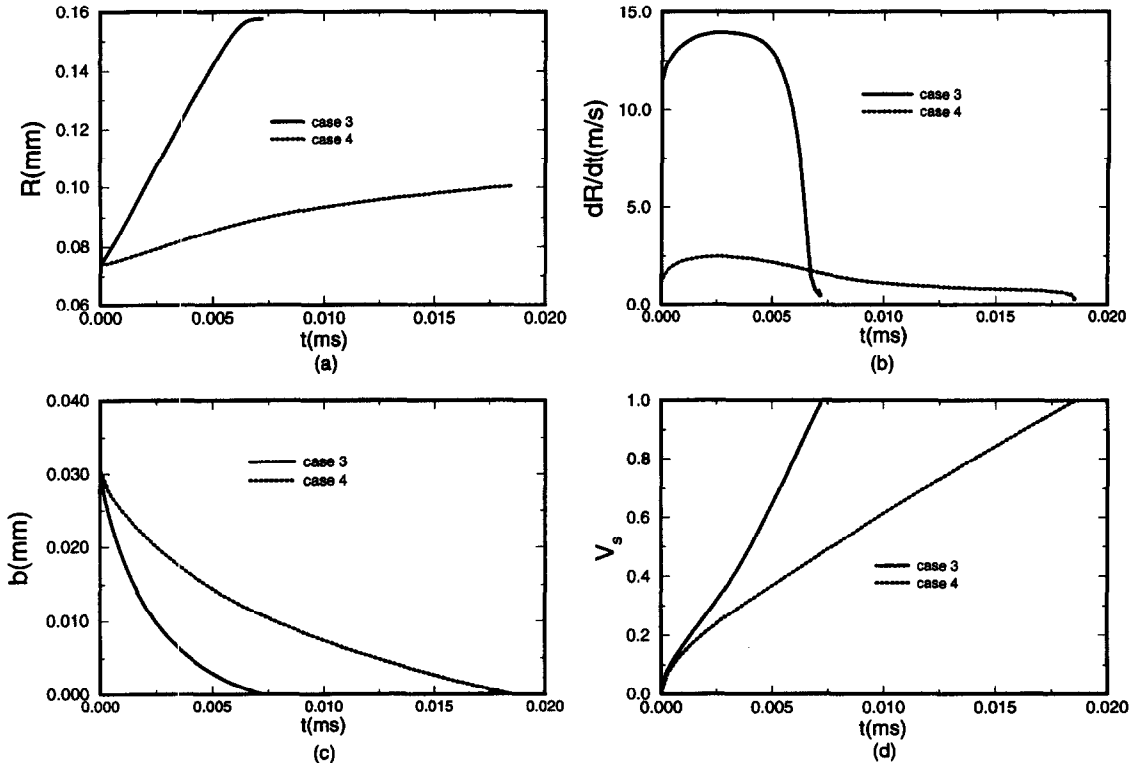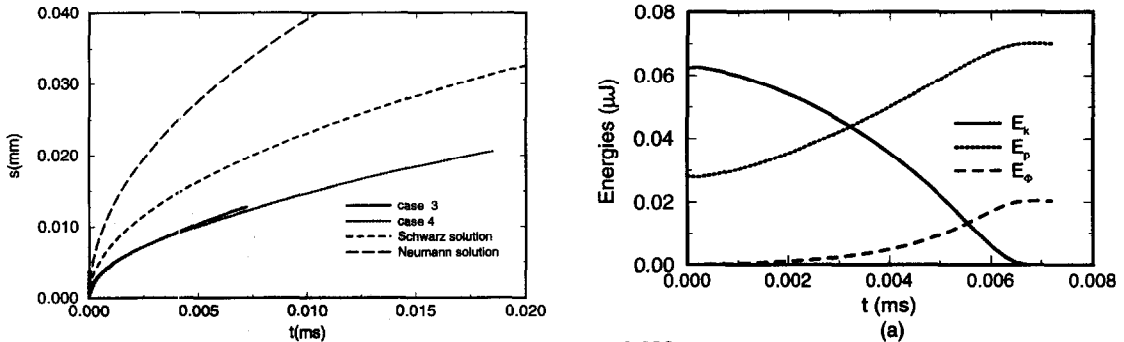energy: (a) case 1 ($w = 10 \text{ m s}^{-1}$); (b) case 2 ($w = 1 \text{ m s}^{-1}$).

Fig. 9. Time evolution of: (a) splat radius; (b) radius expansion rate; (c) liquid thickness; and (d) solid fraction for cases 3 ($w = 10$ m s^{-1}) and 4 ($w = 1$ m s^{-1}).

Fig. 10. Time evolution of the solid-front location along the splat axis for cases 3 ($w = 10$ m s^{-1}) and 4 ($w = 1$ m s^{-1}).

thickness, as measured by the thickness along the axis of the splat, will be reduced. Increasing the droplet size increases the solidification time and the ratio of the final disk radius to the initial droplet diameter, while the ratio of the final centerline solid-thickness to the initial droplet diameter is decreased. In the case of droplet deposition on a sufficiently hot substrate, remelting will take place during the initial stages of the process, and the remelting depth for lower velocities is larger when compared to that for the higher velocity
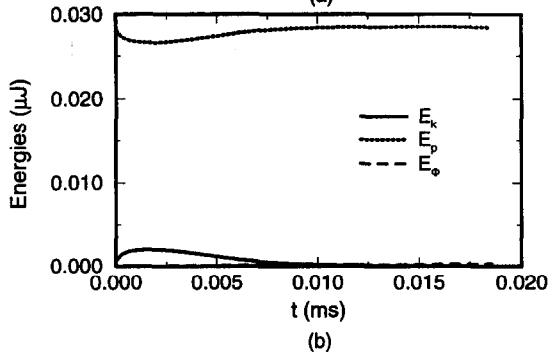

Fig. 11. Time evolution of the liquid-phase mechanical energy: (a) case 3 ($w = 10$ m s^{-1}); (b) case 4 ($w = 1$ m s^{-1}).

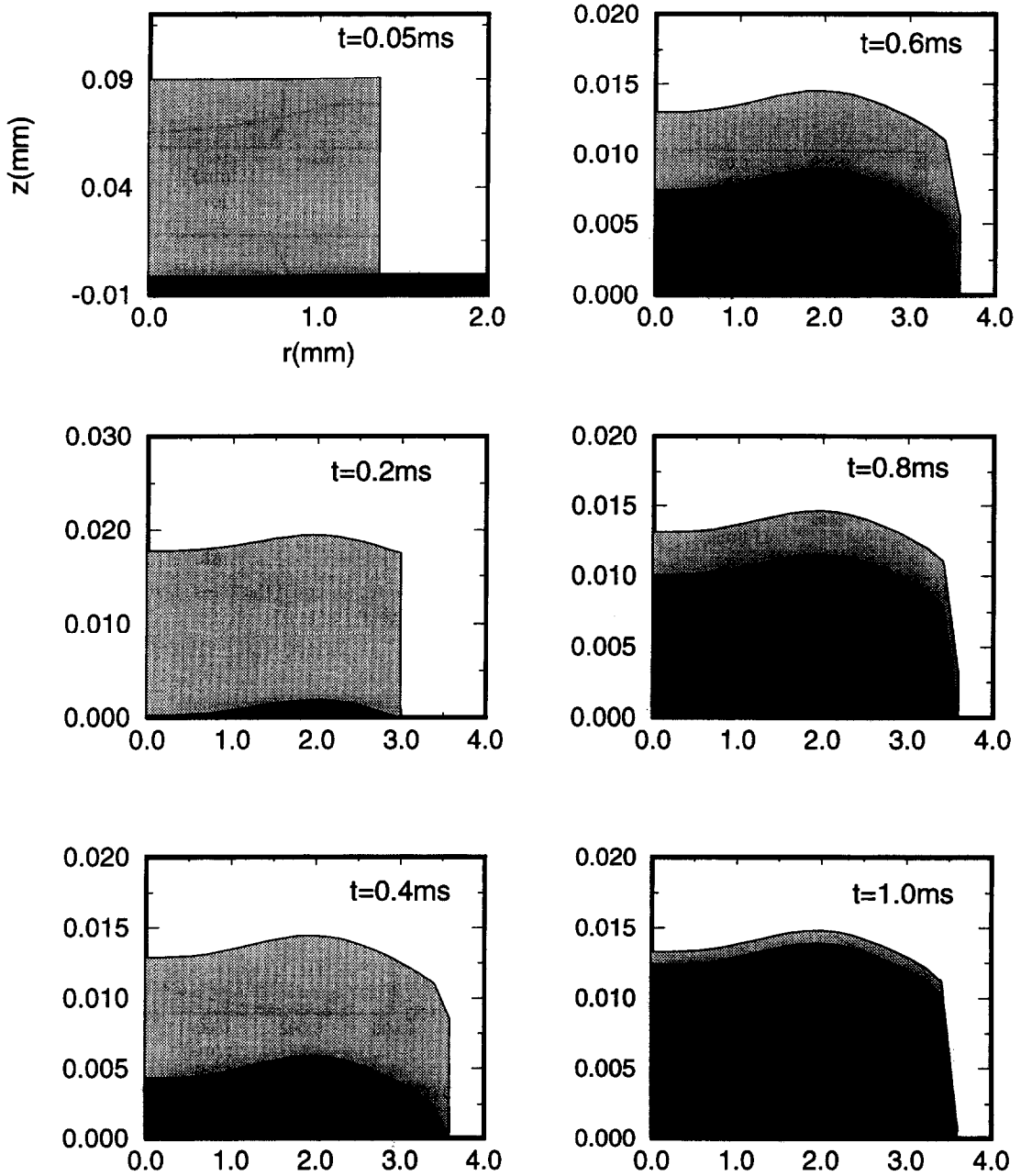Fig. 12. Time evolution of the splat shape for case 5 (dark = solid, gray = liquid) ($d = 1$ mm, $w = 10$ m s^{-1}).
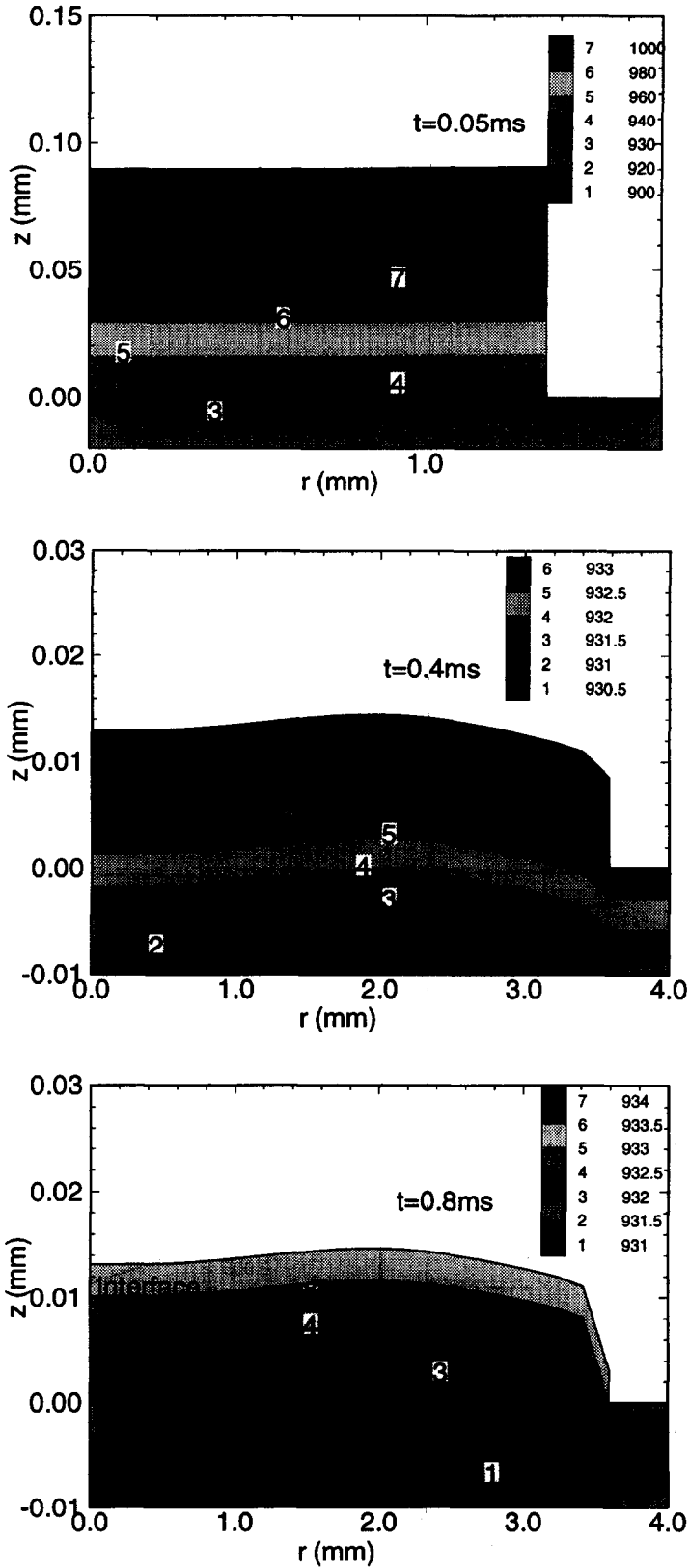
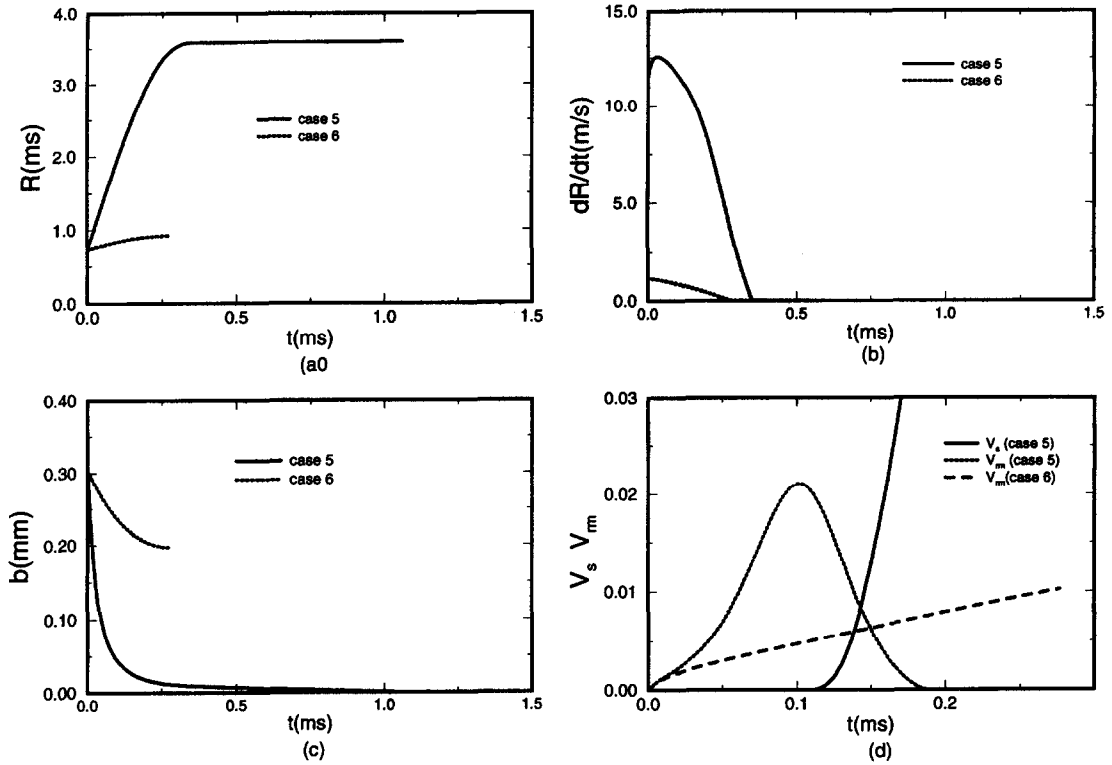Fig. 13. Temperature field in the liquid and upper substrate at selected times (case 5).

Fig. 14. Time evolution of: (a) splat radius; (b) radius expansion rate; (c) liquid thickness; and (d) solid fraction for cases 5 ($w = 10$ m s^{-1}) and 6 ($w = 1$ m s^{-1}).
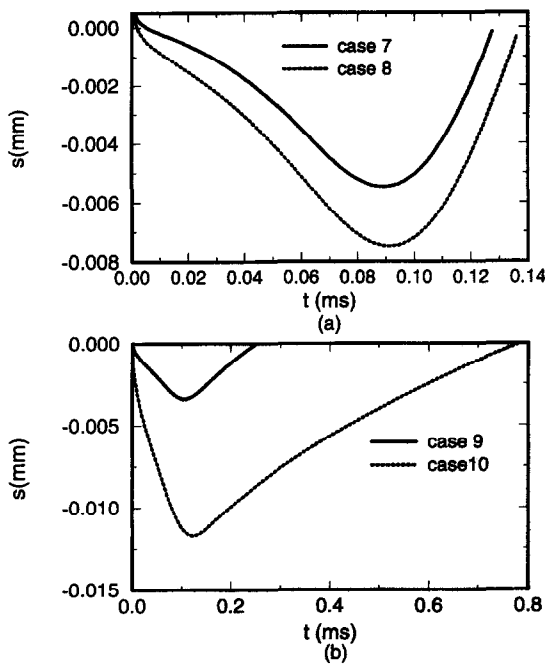

Fig. 15. Time-evolution of solid-front location (remelting front) along the splat axis: (a) cases 7 and 8; (b) cases 9 and 10.
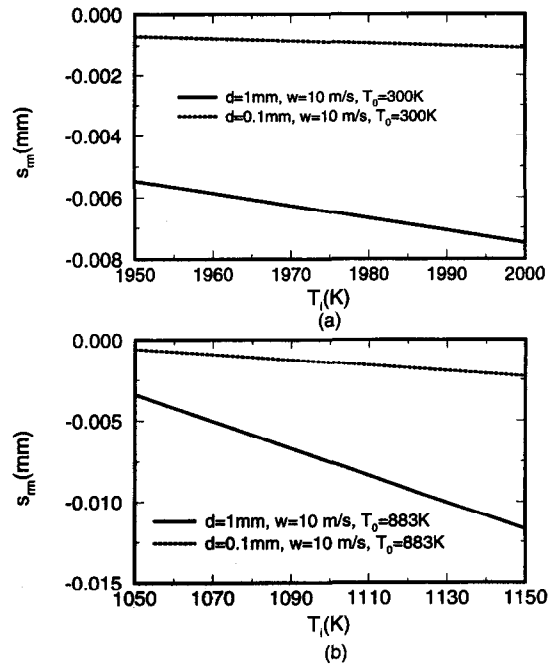
Fig. 16. Variation of maximum remelting depth with initial droplet temperature: (a) deposition on cold substrate (300 K); (b) deposition on hot substrate (883 K).

cases. When remelting occurs, the solidification time is increased significantly. In addition, for higher velocities (10 m s^{-1}), the final splat radius is larger but the final centerline solid-thickness is less for the remelting case as compared to the corresponding cold-substrate case. For lower velocities (1 m s^{-1}), liquid recoiling may occur.

REFERENCES

1. Amon, C. H., Schmaltz, K. S., Merz, R. and Prinz, F. B., Numerical and experimental investigation of interface bonding via substrate remelting of an impinging molten metal droplet. *Transactions of ASME*, 1996, **118**, 164–172.
2. Inada, S. and Yang, W.-J., Solidification of molten metal droplets impinging on a cold surface. *Experimental Heat Transfer*, 1994, **7**, 93–100.
3. Wang, G. X. and Matthys, E. F., Experimental investigation of interfacial conductance for molten metal solidification on a substrate. *Journal of Heat Transfer*, 1996, **118**, 157–163.
4. Liu, W., Wang, G. X. and Matthys, E. F., Thermal analysis and measurements for a molten metal drop impinging on a substrate : cooling, solidification and heat transfer coefficient. *International Journal of Heat and Mass Transfer*, 1995, **38**, 1387–1395.
5. El-Kaddah, N., Mckelliget, J. and Szekely, J., Heat transfer and fluid flow in plasma spraying. *Metallurgy Transaction B*, 1984, **15B**, 59–70.
6. Madejski, J., Solidification of droplets on a cold surface. *International Journal of Heat and Mass Transfer*, 1976, **19**, 1009–1013.
7. Delplanque, J.-P. and Rangel, R. H., An improved model for droplet solidification on a flat surface. *Journal of Materials Science*, 1997 (in press).
8. Markworth, A. J. and Saunders, J. H., An improved velocity field for the Madejski splat-quench solidification model. *International Journal of Heat and Mass Transfer*, 1992, **35**(7), 1836–1837.
9. Watanabe, T., Kuribayashi, I., Honda, T. and Kanzawa, A., Deformation and solidification of a droplet on a cold substrate. *Chemical Engineering Science*, 1992, **47**(12), 3059–3065.
10. San Marchi, C., Liu, H., Lavernia, E. J. and Rangel, R. H., Numerical analysis of the deformation and solidification of a single droplet impinging onto a flat substrate. *Journal of Materials Science*, 1993, **28**, 3313–3321.
11. Liu, H., Lavernia, E. J. and R. H. Rangel, Numerical simulation of substrate impact and freezing of droplets in plasma spray processes. *Journal of Physics D : Applied Physics*, 1993, **26**, 1900–1908.
12. Amon, C. H. and Schmaltz, K. S., Thermal issues in shape deposition manufacturing. *1996 TMS Annual Meeting*, Feb. 4–8, 1996, Anaheim, CA.
13. Waldvogel, J. M., Poulikakos, D., Wallace, D. B. and Marusak, R., Transport phenomena in picoliter size solder droplet dispension. *Transactions of the ASME*, 1996, **118**, 148–156.
14. Kang, B., Zhao, Z. and Poulikakos, D., Solidification of liquid metal droplets impacting sequentially on a solid surface. *Transactions of the ASME*, 1994, **116**, 436–444.
15. Kang, B., Waldvogel, J. and Poulikakos, D., Remelting phenomena in the process of splat solidification. *Journal of Materials Science*, 1995, **30**, 4912–4925.
16. Rangel, R. H. and Bian, X., The inviscid stagnation-flow solidification problem. *International Journal of Heat and Mass Transfer*, 1996, **39**(8), 1581–1602.
17. Rangel, R. H. and Bian, X., Numerical solution of the inviscid stagnation-flow solidification problem. *Numerical Heat Transfer—Part A*, 1995, **28**, 589–603.
18. White, F. M., *Viscous Fluid Flow*, 2nd edn. McGraw-Hill, New York, 1991, p. 153.
19. Fletcher, C. A. J., *Computational Techniques for Fluid Dynamics* 1. Springer, New York, 1988, p. 252.
20. Carslaw, H. S. and Jaeger, J. C., *Conduction of Heat in Solids*, 2nd edn. Clarendon Press, London, 1959, p. 283.

APPENDIX

The metrics of transformation for the liquid phase are :

$$\frac{\partial \theta_l}{\partial \tilde{t}} = \frac{\partial \theta_l}{\partial \tau} + \frac{2}{\pi}\frac{1}{\tilde{b}}\frac{1}{1+\left(\frac{\tilde{z}-\tilde{s}}{\tilde{b}}\right)^2}$$

$$\left[-\frac{\tilde{z}-\tilde{s}}{\tilde{b}}\frac{d\tilde{b}}{d\tau} - \frac{\partial\tilde{s}}{\partial\tau} + \frac{\xi}{\tilde{R}}\frac{\partial\tilde{s}}{\partial\xi}\frac{d\tilde{R}}{d\tau}\right]\frac{\partial\theta_l}{\partial\eta_l}$$

$$-\frac{\xi}{\tilde{R}}\frac{d\tilde{R}}{d\tau}\frac{\partial\theta_l}{\partial\xi} \quad (A.1)$$

$$\frac{\partial\theta_l}{\partial\tilde{r}} = \frac{1}{\tilde{R}}\frac{\partial\theta_l}{\partial\xi} - \frac{2}{\pi}\frac{1}{\tilde{b}}\frac{1}{1+\left(\frac{\tilde{z}-\tilde{s}}{\tilde{b}}\right)^2}\frac{1}{\tilde{R}}\frac{\partial\tilde{s}}{\partial\xi}\frac{\partial\theta_l}{\partial\eta_l} \quad (A.2)$$

$$\frac{\partial\theta_l}{\partial\tilde{z}} = \frac{2}{\pi}\frac{1}{\tilde{b}}\frac{1}{1+\left(\frac{\tilde{z}-\tilde{s}}{\tilde{b}}\right)^2}\frac{\partial\theta_l}{\partial\eta_l} \quad (A.3)$$

$$\frac{\partial^2\theta_l}{\partial\tilde{z}^2} = -\pi\frac{\tilde{z}-\tilde{s}}{\tilde{b}}\left[\frac{2}{\pi}\frac{1}{\tilde{b}}\frac{1}{1+\left(\frac{\tilde{z}-\tilde{s}}{\tilde{b}}\right)^2}\right]^2\frac{\partial\theta_l}{\partial\eta_l}$$

$$+\left[\frac{2}{\pi}\frac{1}{\tilde{b}}\frac{1}{1+\left(\frac{\tilde{z}-\tilde{s}}{\tilde{b}}\right)^2}\right]^2\frac{\partial^2\theta_l}{\partial\eta_l^2}. \quad (A.4)$$

The metrics of transformation for the solid phase are :

$$\frac{\partial\theta_s}{\partial\tilde{t}} = \frac{\partial\theta_s}{\partial\tau} - \frac{\xi}{R}\frac{d\tilde{R}}{d\tau}\frac{\partial\theta_s}{\partial\xi} + \left[\frac{2}{\pi}\frac{c_t}{1+[c_t(\tilde{z}-\tilde{s})]^2}\right]$$

$$-(\tilde{z}-\tilde{s})\frac{d\tilde{b}}{d\tau} - \frac{\partial\tilde{s}}{\partial\tau} + \frac{\xi}{\tilde{R}}\frac{d\tilde{R}}{d\tau}\frac{\partial\tilde{s}}{\partial\xi}\frac{\partial\theta_s}{\partial\eta_s} \quad (A.5)$$

$$\frac{\partial\theta_s}{\partial\tilde{r}} = \frac{1}{\tilde{R}}\frac{\partial\theta_l}{\partial\xi} - \left[\frac{2}{\pi}\frac{c_t}{1+[c_t(\tilde{z}-\tilde{s})]^2}\right]\frac{1}{\tilde{R}}\frac{\partial\tilde{s}}{\partial\xi}\frac{\partial\theta_l}{\partial\eta_l} \quad (A.6)$$

$$\frac{\partial\theta_s}{\partial\tilde{z}} = \left[\frac{2}{\pi}\frac{c_t}{1+[c_t(\tilde{z}-\tilde{s})]^2}\right]\frac{\partial\theta_s}{\partial\eta_s} \quad (A.7)$$

$$\frac{\partial^2\theta_s}{\partial\tilde{z}^2} = \left[\frac{2}{\pi}\frac{c_t}{1+[c_t(\tilde{z}-\tilde{s})]^2}\right]^2\frac{\partial^2\theta_s}{\partial\eta_s^2}$$

$$-\pi c_t(\tilde{z}-\tilde{s})\left[\frac{2}{\pi}\frac{c_t}{1+[c_t(\tilde{z}-\tilde{s})]^2}\right]\frac{\partial\theta_s}{\partial\eta_s}. \quad (A.8)$$

The transformed liquid-phase energy equation is

$$\frac{\partial \theta_l}{\partial \tau} = \frac{1}{RePr}\left[\frac{2}{\pi}\frac{1}{\tilde{b}}\frac{1}{1+\left(\frac{\tilde{z}-\tilde{s}}{\tilde{b}}\right)^2}\right]^2 \frac{\partial^2 \theta_l}{\partial \eta_l^2}$$

$$+\left[\frac{u_r}{\tilde{R}}\frac{\partial \tilde{s}}{\partial \xi} - \frac{\tilde{z}-\tilde{s}}{\tilde{b}}\frac{d\tilde{b}}{d\tau} - \frac{\partial \tilde{s}}{\partial \tau} + \frac{\xi}{\tilde{R}}\frac{\partial \tilde{s}}{\partial \xi}\frac{d\tilde{R}}{d\tau}\right.$$

$$\left. -u_z - \frac{\pi}{RePr}\frac{\tilde{z}-\tilde{s}}{\tilde{b}}\frac{2}{\pi}\frac{1}{\tilde{b}}\frac{1}{1+\left(\frac{\tilde{z}-\tilde{s}}{\tilde{b}}\right)^2}\right]\frac{2}{\pi}\frac{1}{\tilde{b}}\frac{1}{1+\left(\frac{\tilde{z}-\tilde{s}}{\tilde{b}}\right)^2}\frac{\partial \theta_l}{\partial \eta_l}$$

$$+\left(\frac{\xi}{\tilde{R}}\frac{d\tilde{R}}{d\tau} - \frac{u_r}{\tilde{R}}\right)\frac{\partial \theta_l}{\partial \xi} + \frac{Ec}{Re}\Phi\theta_i \qquad (A.9)$$

with boundary conditions: $\theta_l = 0$ at $\eta = 0$, $\partial\theta_l/\partial\eta_l = 0$ at $\eta = 0.5$, $\partial\theta_l/\partial\xi = 0$ at $\xi = 0$, and

$$\frac{1}{\tilde{R}}\frac{\partial \theta_l}{\partial \xi} - \frac{2}{\pi}\frac{1}{\tilde{b}}\frac{1}{1+\left(\frac{\tilde{z}-\tilde{s}}{\tilde{b}}\right)^2}\frac{1}{\tilde{R}}\frac{\partial \tilde{s}}{\partial \xi}\frac{\partial \theta_l}{\partial \eta_l} = 0 \quad \text{at } \xi = 1.$$

The transformed solid-phase energy equation is

$$\frac{\partial \theta_s}{\partial \tau} = \frac{1}{a_\alpha RePr}\left[\frac{2}{\pi}\frac{c_t}{1+[c_t(\tilde{z}-\tilde{s})]^2}\right]^2 \frac{\partial^2 \theta_s}{\partial \eta_s^2}$$

$$+\left\{(\tilde{z}-\tilde{s})\frac{d\tilde{b}}{d\tau} + \frac{\partial \tilde{s}}{\partial \tau} - \frac{\xi}{\tilde{R}}\frac{d\tilde{R}}{d\tau}\frac{\partial \tilde{s}}{\partial \xi}\right.$$

$$\left. -\frac{\pi(\tilde{z}-\tilde{s})}{a_\alpha RePr}\left[\frac{2}{\pi}\frac{c_t}{1+[c_t(\tilde{z}-\tilde{s})]^2}\right]\right\}\left[\frac{2}{\pi}\frac{c_t}{1+[c_t(\tilde{z}-\tilde{s})]^2}\right]\frac{\partial \theta_s}{\partial \eta_s}$$

$$+\frac{\xi}{\tilde{R}}\frac{d\tilde{R}}{d\tau}\frac{\partial \theta_s}{\partial \xi} \qquad (A.10)$$

with boundary conditions: $\theta_s = -1$ at $\eta = -1$, $\partial\theta_s/\partial\eta_s = 0$ at $\eta = 0$, $\partial\theta_l/\partial\xi = 0$ at $\xi = 0$, and

$$\frac{1}{\tilde{R}}\frac{\partial \theta_l}{\partial \xi} - \left[\frac{2}{\pi}\frac{c_t}{1+[c_t(\tilde{z}-\tilde{s})]^2}\right]\frac{1}{\tilde{R}}\frac{\partial \tilde{s}}{\partial \xi}\frac{\partial \theta_l}{\partial \eta_l} = 0 \quad \text{at } \xi = 1.$$

The interface energy-balance equation is transformed into

$$\frac{\partial \tilde{s}}{\partial \tau} = \frac{\xi}{\tilde{R}}\frac{d\tilde{R}}{d\tau}\frac{\partial \tilde{s}}{\partial \xi} + \frac{St}{RePr}\left[1+\left(\frac{1}{\tilde{R}}\frac{\partial \tilde{s}}{\partial \xi}\right)^2\right]\left[\frac{2}{\pi}c_t\frac{\partial \theta_s}{\partial \eta_s} - \frac{2}{\pi}\frac{1}{\tilde{b}}a_k\frac{\partial \theta_l}{\partial \eta_l}\right].$$

$$(A.11)$$